

---

1        **Equatorial Plasma Bubbles Developing Around Sunrise**  
2        **Observed by an All-Sky Imager and GNSS Network during**  
3        **the Storm Time**

4  
5        Kun Wu<sup>1,2</sup>, Jiyao Xu<sup>1,2</sup>, Xinan Yue<sup>3,2</sup>, Chao Xiong<sup>4</sup>, Wenbin Wang<sup>6</sup>, Wei Yuan<sup>1,2</sup>, Chi  
6        Wang<sup>1,2</sup>, Yajun Zhu<sup>5</sup>, Ji Luo<sup>1,2</sup>

7  
8        <sup>1</sup>State Key Laboratory of Space Weather, National Space Science Center, Chinese Academy of  
9        Sciences, Beijing, China

10       <sup>2</sup>College of Earth and Planetary Sciences, University of Chinese Academy of Sciences, Beijing,  
11       China

12       <sup>3</sup>Key Laboratory of Earth and Planetary Physics, Institute of Geology and Geophysics, Chinese  
13       Academy of Sciences, Beijing, China

14       <sup>4</sup>GFZ German Research Centre for Geosciences, Telegrafenberg, 14473 Potsdam, Germany.

15       <sup>5</sup>Institute of Energy and Climate Research (IEK-7), Forschungszentrum Juelich GmbH, Juelich,  
16       Germany

17       <sup>6</sup>High Altitude Observatory, National Center for Atmospheric Research, Boulder, CO, USA

18  
19  
20       Correspondence to: [jyxu@spaceweather.ac.cn](mailto:jyxu@spaceweather.ac.cn)

21  
22  
23       *Keywords:* Equatorial plasma bubble near sunrise, Spread-F, All-sky imager, GNSS  
24       network

---

27 **Abstract.**

28 A large number of studies have shown that equatorial plasma bubbles (EPBs) occur  
29 mainly after sunset, and they usually drift eastward. However, in this paper, an unusual  
30 EPB event was simultaneously observed by an all-sky imager and the Global  
31 Navigation Satellite Systems (GNSS) network in southern China, during the recovery  
32 phase of geomagnetic storm happened on 6-8 November 2015. Observations from both  
33 techniques show that the EPBs appeared near dawn. Interestingly, the observational  
34 results show that the EPBs continued to develop after sunrise, and disappeared about  
35 one hour after sunrise. The development stage of EPBs lasted for at least about 3 hours.  
36 To our knowledge, this is the first time that the evolution of EPBs developing around  
37 sunrise was observed by an all-sky imager and the GNSS network. Our observation  
38 showed that the EPBs drifted westward, which was different from the usually eastward  
39 drifts of post-sunset EPBs. The simulation from TIE-GCM model suggest that the  
40 westward drift of EPBs should be related to the enhanced westward winds at storm time.  
41 Besides, ~~break~~[bifurcation](#) and ~~recombination~~[merging](#) processes of EPBs were observed  
42 by the all-sky imager in the event. Associated with the development of EPBs, increasing  
43 in the ionospheric F region peak height was also observed near sunrise, and we suggest  
44 the enhance upward vertical plasma drift during geomagnetic storm plays a major role  
45 in triggering the EPBs near sunrise.

46

47 **1. Introduction**

48 After sunset, plasma density depletions, also called equatorial plasma bubbles (EPBs),  
49 sometime occur in the equatorial- and low-latitude ionosphere. A large number of  
50 studies have shown that EPBs generally start to develop shortly after sunset during  
51 geomagnetic quiet periods (e.g., Weber et al., 1980; Kelley et al., 1986; Xiong et al.,  
52 2010; Wu et al., 2018). It is generally believed that the Rayleigh-Taylor instability (RTI)  
53 is a plausible mechanism to trigger the EPBs (Kelley, 2009; Makela ~~&~~[and](#) Otsuka,  
54 2012). The growth rate of RTI is influenced by a number of different factors, such as  
55 the zonal electric field, neutral wind and the ~~background~~

---

56 ~~ionospheric/thermosphere~~[vertical gradient of plasma density at the bottomside of the F](#)  
57 [region or ion-neutral collision frequency](#), as well as the strength of magnetic fields (Ott,

58 1978; Abdu, 2001; Burke et al, 2004). The pre-reversal enhancement (PRE) of the  
59 eastward electric field around sunset is a main reason for the development of EPBs (e.g.,  
60 Fejer et al., 1999; Abdu, 2001; Kelley, 2009; Huang, 2018). Owing to the intensified  
61 eastward electric field, near magnetic equator the ionosphere is rapidly elevated to  
62 higher altitudes via  $E \times B$  drifts, which is favorable for the growth of RTI at the  
63 bottomside of the ionosphere.

64 The EPBs are thought to extend along magnetic field lines, and can reach as high as  
65 magnetic latitudes of about  $\pm 20^\circ$  (Kelley, 2009; Lühr et al., 2014). Xiong et al. (2016,  
66 2018) suggest that EPBs have a typical zonal size of about 50 km, by using Swarm in  
67 situ electron density measurements as well as ground-based airglow imager. Although  
68 the characteristics of EPBs have been widely studied, special events, especially those  
69 occurring during geomagnetic storms, are still one of the interesting issues to be fully  
70 addressed. Some of the results showed that geomagnetic storms can affect the  
71 development of EPBs (e.g., Abdu et al., 2003; Tulasi et al., 2008; Carter et al., 2016),  
72 and in some extreme cases, the EPBs can extend to middle latitudes during intense  
73 geomagnetic storms (e.g., Sahai et al., 2009; Patra et al., 2016; Katamzi-Joseph et al.,  
74 2017; Aa et al., 2018). Moreover, in the storm time, EPBs near sunrise were  
75 occasionally observed by some instruments such as radar and satellite. Fukao et al.  
76 (2003) used observations from the Equatorial Atmosphere Radar to report EPBs near  
77 sunrise over the Indonesian region during a geomagnetic storm and suggested that the  
78 EPBs were likely associated with the geomagnetic storm. Huang et al. (2013) reported  
79 the observations of long-lasting daytime EPBs with the Communications/Navigation  
80 Outage Forecasting System (C/NOFS) satellite during a geomagnetic storm in which  
81 the EPBs were persistent from the post-midnight sector through the afternoon sector.  
82 Zhou et al. (2016) used observations from multiple low Earth orbiting satellites, like  
83 the Swarm constellation, the Gravity Recovery and Climate Experiment (GRACE)  
84 satellite, and the C/NOFS satellite, to detect the EPBs around sunrise during the St

---

85 Patrick's Day storm. They suggested that the geomagnetic storm induced changes in  
86 ionospheric dynamics should be the reason for triggering the EPBs. But until now, there  
87 has been no research on the occurrence characters and evolution of EPBs around sunrise  
88 using optical remote sensing, which can provide different aspects of the EPBs near  
89 sunrise.

90 It is well known that the EPBs usually drift eastward as reported by many studies (e.g.,  
91 Pimenta et al., 2001; Martinis et al., 2003; Park et al., 2007; Taylor et al., 2013; Wu et  
92 al., 2017). However, during storm periods westward drifting EPBs have been also  
93 observed (Abdu et al., 2003; Basu et al., 2010; Santos et al., 2016). Abdu et al. (2003)  
94 reported some cases of EPBs that showed eastward drifts after sunset and later reversed  
95 to westward. Basu et al. (2010) reported that the westward drifting EPBs reached  
96 maximum velocities of about 80 - 120 m/s. Santos et al. (2016) also showed some EPBs  
97 of zonal drifts reversal (eastward to westward) during a geomagnetic storm, ~~in~~  
98 ~~which~~ and they suggested the [reversal was caused by a vertical Hall electric field](#) ~~caused~~  
99 [which induced by a zonal prompt penetration electric field \(PPEF\) in the](#) ~~reversal.~~  
100 [presence of enhanced conductivity in the E region during night.](#)

101 From six-year observations of airglow image located in the southern China, we found  
102 only one case of EPBs starting to appear near sunrise during the storm recovery phase  
103 on 08 November 2015. The EPBs appeared before sunrise, kept developing and  
104 vanished in about 1 hour after sunrise. Unlike the quiet-time eastward drifting EPBs,  
105 the EPBs drifted westward. In the rest, we provide a detailed analysis of this event. In  
106 section 2, we give a general description of the instruments. Observational results are  
107 showed in section 3. In section 4, we provide comparisons with previous studies as well  
108 as discussions. Finally, summary is given in section 5.

109

## 110 **2. Instrumentation**

### 111 **2.1 All-sky imager**

112 The airglow data used in this study are obtained from an all-sky imager, which is  
113 deployed at Qujing, China (Geographic: 25° N, 104° E; Geomagnetic: 15.1° N, 176°

---

E). Its location is indicated by the red star in Figure 1, and the blue circle represents the [projected regions with a radius of ~900 km \(about 140° field of view \(FOV\)\)](#) of the all-sky imager at an altitude of 250 km. The all-sky imager consists of a CCD detector (1024 × 1024 pixel), an interference filter (630.0 nm), and a fish-eye lens (FOV of 180°). The integration time of the all-sky imager is 3 min.

## 2.2 The Network of Global Navigation Satellite System (GNSS)

The GNSS data used in this study are derived from the Crustal Movement Observation Network of China (CMONOC), which consists of ~260 ground GNSS receivers covering the mainland of China. The information of these GNSS receivers has been given in previous publications (e.g., Aa et al., 2015; Yang et al., 2016; Zheng et al., 2016). The [residuals of](#) total electron content (TEC) was processed using the similar method as that described by Ding et al. (2014). Specifically, for each arc, the relative phase TEC was filtered using a band-pass filter. [The minimum and maximum period of the band-pass filter was 2 min and 12 min respectively.](#) We then calculated the TEC residual of each arc for each pierce point, which the height of each ionospheric pierce point was about 300 km. Therefore, the TEC residual could indicate the occurrence of plasma bubbles. An elevation cutoff angle of 30° is used to reduce the multi-paths effects. [Besides, to better present the structure of EPBs, the rate of TEC change index \(ROTI\) was also calculated. The ROTI is the standard deviation of the TEC gradient, which is rate of TEC change \(ROT\). Based on  \$\(TEC\(t+\Delta t\)-TEC\(t\)\)/\Delta t\$ , we can get the ROT. In the study, we used  \$\Delta t=30s\$  to calculate the ROT and used 10 ROT to get 5 min ROTIs. Similar calculation of ROT and ROTI have already been reported and discussed by many previous studies \(e.g., Pi et al., Otsuka et al., 2006; Buhari et al., 2004\), we will not be described in here.](#)

## ~~2.3 Digisond~~

## 2.3 Digisonde

The digisonde ionograms are obtained from a digisonde located at Fuke, a low-latitude

---

143 station in the southern China (Geographic: 19.5° N, 109.1° E; Geomagnetic: 9.5° N,  
144 178.4° W), and marked with a green dot in Figure 1. The virtual heights of the *F* layer  
145 were manually scaled by using the SAO Explorer software.

146

### 147 **3. Observations and Results**

148 Figure 2 shows the 3-hour *Kp* index, the interplanetary magnetic field (IMF) *Bz*, *SYM-*  
149 *H*, AE, AU, AL and h' F at Fuke on 06-08 November 2015. To make the comparison  
150 easier with other observations, we converted the universal time to the local time (LT)  
151 at Qujing. A geomagnetic storm occurred during those days. In Figure 2(b), IMF *Bz*  
152 turned southward at ~11:40 LT on 07 November 2015, and reached to about -11 nT at  
153 ~16:00 LT. During the storm main phase, the *SYM-H* had a rapid reduction from -40 nT  
154 to -100 nT. Meanwhile, the *Kp* index reached a value of 6; the AE and AL also reached  
155 at ~1500 nT and ~- 1500 nT, respectively. After 04:00 LT on 08 November 2015, IMF  
156 *Bz* began to turn to north. In the storm recovery phase, the value of *SYM-H* was back to  
157 -40 nT.

158 Figure 3 shows the time sequence of airglow images observed by the all-sky imager at  
159 Qujing from 05:15 to 06:21 LT on 8 November 2015. The time difference between  
160 successive images is 6 min. For each image, we removed the effects of compression  
161 and curving of the all-sky imager lens by an unwarping process (Garcia et al., 1997).  
162 All images have been mapped into a geographic range from 97° to 111° E in longitude  
163 and from 18° to 32° N in latitude. The height of the airglow layer is assumed to be at  
164 250 km. The top of each image is to the north and the right to the east. Two EPBs,  
165 marked as “b1” and “b2”, were observed by the all-sky imager during this period. They  
166 occurred during the geomagnetic storm recovery phase.

167 Around 05:21 LT, EPB “b1” appeared in the FOV of the all-sky imager. “b1” was still  
168 developing, as it extended northward and reached close to 25° N around 06:21 LT. At  
169 05:39 LT, the other EPB “b2” started to appear in the FOV of the airglow imager. “b2”  
170 was also developing and expanded to about 20° N at 06:21 LT. The two observed EPBs  
171 possibly continued to develop after 06:21 LT, as no hints of stop can be seen in the last

---

172 airglow image. However, there was no further image data after 06:21 LT because the  
173 all-sky imager had to be shut down after sunrise. We want to pointed out that the sunrise  
174 time at Qujing was around 06:15 LT at altitude of 250 km on that day. The far north  
175 part of “b1” reached about 24.5°N at 06:15 LT. After 6 min, the far north of “b1”  
176 extended to about 25°N (as marked by the black horizontal line). In other words, the  
177 observational result from the all-sky imager suggested that the EPBs kept developing  
178 after sunrise.

179 Some interesting features can also be seen from Figure 3. “b1” appeared at ~105° E and  
180 “b2” appeared at ~104° E at 05:39 LT. Based on the black vertical line at 106° E, we  
181 can clearly see that the two EPBs drifted from east to west. Besides, ~~break~~bifurcation  
182 and ~~recombination~~merging processes of EPB “b1” were also observed. After 05:45 LT,  
183 a ~~break~~bifurcation process occurred in “b1”. The lower latitude portion of “b1” moved  
184 further to the westward. An obvious cleft occurred at ~19° N of “b1” near 06:03 LT.  
185 More interesting is the fact that a ~~recombination~~merging process occurred in the two  
186 ~~break~~bifurcation portions of “b1” during its later development period. After ~06:03 LT,  
187 the upper portion of “b1” began to connect to the lower portion of “b1” and they  
188 merged/combined together into one EPB after 06:15 LT. The ~~break~~bifurcation and  
189 ~~recombination~~merging processes are more obvious in the red rectangles of Figure 3,  
190 which is indicated by the red arrow in each image.

191 Figure 4 shows a series of TEC residuals over 10°-50°N and 80°-130°E during 04:30-  
192 08:20 LT on 08 November 2015. The adjacent imaging is in 10 min intervals. At about  
193 04:40 LT, some TEC depletions, which occurred to the south and west of the location  
194 of all-sky imager, appeared at ~115°E (~24°N), and began to develop. About 05:30 LT,  
195 some additional EPBs appeared at ~105°E (~20°N), and they were also developing.  
196 EPBs in the two regions kept developing until they disappeared. Owing to the FOV of  
197 the all-sky imager, the EPBs outside the ~115°E region were not observed.

198 In order to provide much more detailed comparison between the all-sky imager and  
199 TEC measurements, we ~~chose those~~give local time variation of the absolute TEC  
200 ~~variations of~~after 05:15 LT (Figure 5) which corresponding geographical area ~~and time~~

---

201 of ~~each~~ airglow imaging of ~~Figure 3 in Figure 5~~. In Figure 5, the TEC ~~variations show~~  
202 ~~that the EPBs~~ depletions at  $\sim 105^\circ$  E appeared near 05:30 LT, which correspond to EPB  
203 “b1” and “b2” observed by the all-sky imager. ~~In Figure 5,~~ And after  $\sim 07:45$  LT, those  
204 TEC depletions disappeared. For a better representation, we showed ROTI variations  
205 which correspond geographical area and time of each airglow imaging of Figure 3. In  
206 Figure 6, the ROTI enhancement at  $\sim 105^\circ$  E also correspond to EPB “b1” and “b2”  
207 observed by the all-sky imager near 05:30 LT. The ROTI enhancement move away from  
208 the  $106^\circ$  E with time (The black vertical line represents the  $106^\circ$  E in Figure ~~5~~6), which  
209 is consistent with the movement of EPBs observed by the airglow imager. Meanwhile,  
210 the northernmost part of the ~~depletion of  $\sim 105^\circ$  E~~ ROTI enhancement expanded to  
211  $\sim 25^\circ$  N at 06:~~20~~21 LT (The black horizontal line represents the  $25^\circ$  N in Figure ~~5~~6),  
212 which also agreed well with the observations of the all-sky imager. Interestingly, In  
213 Figure 4, TEC ~~variations~~ residuals show that the northernmost of EPBs of  $\sim 105^\circ$  E  
214 extended beyond  $25^\circ$  N after 06:20 LT. We can see that the northernmost of them  
215 reached about  $28^\circ$  N at 07:10 LT ~~in Figure 4~~. In other words, TEC variations show that  
216 ~~the~~ those depletions ~~of  $\sim 105^\circ$  E~~ were still ~~there~~ existence after 06:21 LT, and kept  
217 developing after sunrise, but vanished ~~after~~ near  $\sim 08:00$  LT. These observational results  
218 shown that the life time of those EPBs exceeds 3 hours.

#### 220 4. Discussion

221 In this study we showed an special event of EPBs which was simultaneously observed  
222 by the all-sky imager and the ground GNSS network in the south China. One interesting  
223 feature is that the EPBs started to appear near sunrise hours. Afterward, they kept  
224 developing until they totally vanished. During their life time, the EPBs moved from  
225 east to west. Those EPBs occurred in the recovery phase of the geomagnetic storm,  
226 which indicates that the prompt penetration electric fields (PPEF) and disturbance  
227 dynamo (~~DDEF~~),<sub>2</sub> as well as disturbed neutral wind circulation may play an import role  
228 in triggering the EPBs.

229 The drift velocities of EPBs were shown in Figure ~~6~~7. We used the cross sections  
230 (keogram) (Figures ~~6~~7 (a), (c), and (e)) of the airglow images to separately calculate



---

231 meridian velocities (Figure 67(b)) of “b1” and zonal velocities of “b1” at  $\sim 22^\circ\text{N}$   
232 (Figure 67(d)) and  $\sim 19^\circ\text{N}$  (Figure 67(f)) geographical latitudes. Figure 67(a) illustrates  
233 the N-S cross sections (between  $104^\circ\text{E}$  and  $105^\circ\text{E}$ ) of the airglow images shown in  
234 Figure 3. Figure 67(c) illustrates the W-E cross sections (between  $21.5^\circ\text{N}$  and  $22^\circ\text{N}$ ) of  
235 the airglow images, and Figure 67(e) illustrates the W-E cross sections (between  $18.5^\circ\text{N}$   
236 and  $19^\circ\text{N}$ ).

237 We separately calculated poleward and zonal velocities of “b1” based on the position  
238 of it changed over time in Figure 67(a), Figure 67(c) and Figure 67(e). The initial  
239 poleward and zonal velocities of “b1” were about 200 m/s and 60 m/s, respectively.  
240 Horizontal drift of EPB is also an important issue, which is often related to the  
241 background zonal plasma drift (Fejer et al., 2005; Eccles, 1998). The westward motion  
242 of the F-region should be caused by the ionospheric dynamo process in the early  
243 morning (Kil et al., 2000; Sheehan & Valladares, 2004). The drift direction of  
244 background zonal plasma drift has a reversal (eastward to westward) near dawn (Fejer  
245 et al., 2005). [Huang and Roddy. \(2015\) also found the drift velocity of EPBs was  
246 eastward at night and reverses to westward near dawn by using data from C/NOFs and  
247 they showed enhanced geomagnetic activities caused a westward EPB drift in the  
248 nighttime through disturbance dynamo process.](#) In our case, all EPBs emerged after  
249 05:00 LT. The background plasma should drift westward during the early morning hours.  
250 So, it could partly explain why the observed EPBs drifted westward. In addition, the  
251 disturbed westward neutral winds can also contribute to the westward drifting of EPBs.  
252 Xiong et al. (2015) found that the disturbance winds were mainly towards westward at  
253 low latitudes, most prominent during early morning hours. Abdu et al. (2003) found  
254 that the westward drift of an EPB was most likely caused by westward zonal winds  
255 during a geomagnetic storm. Makela et al. (2006) found that the eastern wall of EPBs  
256 can become unstable due to the westward and equatorward neutral winds associate with  
257 wind surges. [When the wind blow westward, and thus the wind-induced Pedersen  
258 current flows downward, gradient-drift instability can occur at the eastern wall of EPB,  
259 where the plasma density gradient is eastward. So, secondary instabilities are more](#)

---

260 [likely to occur at eastern wall of EPBs.](#) In Figure 3, a sub-branch of dark bands first  
261 occurred at the eastern wall of “b1”, indicated secondary instabilities developed at the  
262 eastern edge, most likely due to the westward disturbance winds.

263 In Figure [78](#), we used the Thermosphere-Ionosphere-Electrodynamics General  
264 Circulation Model (TIE-GCM) to simulate the horizontal winds on 08 November 2015  
265 under magnetically active conditions, and the latitude versus longitude distribution of  
266 zonal wind velocities are shown at different times. The winds at 250 km are shown, and  
267 the spatial coverage has been confined to 0° - 40° N latitude and 90° - 120° E longitude.  
268 The dashed rectangles represent the location of “b1” and “b2” at different times. In  
269 Figure [78](#), we can see that the horizontal winds at low latitudes are mainly westward,  
270 which is consistent with the motion of EPBs in this case. As already discussed above,  
271 the westward drift of those EPBs is possibly caused by the westward disturbance winds.  
272 Besides, the zonal winds computed from TIE-GCM shown in Figure [78](#) are smaller  
273 than the zonal drifts of EPBs shown in Figure [67](#). This is because zonal drift value of  
274 EPBs was controlled by background zonal winds and ionospheric electric field  
275 (Haerendel et al., 1992; Eccles, 1998). The value differences between simulation and  
276 zonal drifts of EPBs should be influenced by ionospheric electric field. [Besides, The](#)  
277 [difference between the model simulated background zonal winds and the derived zonal](#)  
278 [drifts of EPBs from airglow images is possibly due to that the model simulation provide](#)  
279 [mainly reflect a general trend of the wind, but not the exact wind velocity in reality.](#)

280 As reported, most of the EPBs start to occur at pre-midnight hours. There were a very  
281 limited number of studies that used data from radar or satellite to report the occurrence  
282 of EPB close to sunrise hours (e.g., Fukao et al., 2003; Huang et al., 2013; Zhou et al.,  
283 2016). However, until now, there has been no observation result of EPBs around sunrise  
284 using optical remote sensing. In fact, it is very difficult to observe EPB near sunrise by  
285 an all-sky imager. Often, EPBs start to develop shortly after sunset and vanish before  
286 sunrise. Even though some EPBs occur around sunrise in their initial stage, they  
287 disappear when they drift eastward into the daytime. And almost no report shows that  
288 the EPBs still kept developing after sunrise. In our case, the developing EPB was first

---

289 observed at about 05:30 LT (near dawn) by both the all-sky imager and the GNSS  
290 network. [The local time variation of absolute TEC showed that EPBs existed after](#)  
291 [sunrise and they disappeared after 07:45 LT.](#) Our observational results show that they  
292 kept developing after sunrise, and vanished about one hour after sunrise. Those EPBs  
293 should be occurred near sunrise, which is different from post-sunset EPBs. Their  
294 development stages lasted for at least about 3 hours.

295 In the rest, we try to explain why the EPBs occurred near sunrise. During the storm  
296 time, disturbance winds can affect the low-latitude ionospheric electrodynamics as well  
297 as the zonal drift of an EPB. The DDEF [caused by storm](#) will drive plasma drift to move  
298 upward ~~at~~[during](#) nighttime ~~during the development phase of storm~~ (Blanc and  
299 Richmond, 1980). Meanwhile, a number of studies found the that high latitude electric  
300 fields can penetrate into the middle and low-latitude ionosphere as PPEF when IMF  $B_z$   
301 turns southward or northward (Kelley et al., 1979; Scherliess and Fejer, 1997; Cherniak  
302 [&and](#) Zakharenkova, 2016; Carter et al., 2016; Patra et al., 2016; Katamzi-Joseph et al,  
303 2017). For the storm event, after IMF  $B_z$  turned southward at ~12:00 LT 07 November  
304 2015, there was long duration and high AE in storm time. A DDEF should be present  
305 at recovery phase of storm time. And it reversed ambient electric field from westward  
306 to eastward near sunrise, which enhanced height of bottomside of the ionosphere  $F$ -  
307 region. Meanwhile, the northward turning of IMF  $B_z$  at ~04:00 LT 08 November 2015  
308 caused over- shielding electric field, which produced an eastward PPEF into the low-  
309 middle latitude ionosphere. The eastward electric field also moved the  $F$  region  
310 ionosphere to higher altitudes via vertical  $E \times B$  drifts. In Figure 2(e), the increased  
311 height of bottomside of the ionosphere  $F$ -region can be seen at Fuke. In low latitude  
312 region, one of the necessary conditions for the generation of EPBs is that the  $F$  layer  
313 should be uplifted to a higher altitude, where the RTI becomes unstable and forms EPBs.  
314 The  $F$  layer height is largely determined by the eastward field via the vertical  $E \times B$  drift  
315 (Dabas et al., 2003).

316 In this study, EPBs were initially observed by the all-sky imager at about 05:15 LT. We  
317 think that only a portion of the EPBs were observed in our study, as EPB usually extend

---

318 along the whole magnetic flux-tube. It also means that the EPBs should possibly occur  
319 before 05:15 LT at equatorial latitude. But due to the lack of observations at equator,  
320 we cannot provide direct evidence about their generation. However, as shown in our  
321 Figure 89, we also found that spread  $F$  began to appear in the ionograms from the  
322 digisonde at Fuke after 05:15 LT, which indicates that those EPBs occurred in the region  
323 of southeastern Qujing (Note that Fuke is to the southeast of Qujing). Bottomside of  
324 the ionospheric F-region at Fuke was rapidly elevated from  $\sim 250$  km to  $\sim 290$  km near  
325 sunrise on 08 November 2015. The rapidly elevated height of the ionosphere can cause  
326 stronger RTI at the bottom of the ionosphere F-region, which is beneficial to the  
327 formation of EPB. The initial occurring time of EPBs of this case should be during this  
328 time. Unfortunately, we do not have more observations in the southeast of Fuke. We  
329 used the TIE-GCM to simulate the height of hmF2 at lower latitude on 08 November  
330 2015. Figure 910 shows the hmF2 as a function of longitude and latitude at different  
331 times. The model results plotted are in a geographic range from  $0^\circ$  to  $40^\circ$  N in latitude  
332 and from  $90^\circ$  to  $120^\circ$  E in longitude. In Figure 910, we can see that hmF2 southeast of  
333 (the dashed rectangles) Qujing was rapidly elevated to higher altitudes near sunrise. In  
334 other words, when the IMF  $B_z$  turned northward at about 04:00 LT, the ionosphere in  
335 some regions southeast of Qujing could be rapidly elevated to higher altitudes at this  
336 time. Those EPBs occurred in the same time period as highlighted by the green  
337 rectangular area in Figure 2. Previous studies have reported that the occurrence of the  
338 dawn enhancement in the equatorial ionospheric vertical plasma drift (Zhang et al.,  
339 2015, 2016). They found that the enhancement of the ionospheric vertical plasma drift  
340 occurs around dawn. They suggested that the vertical plasma drifts can be enhanced  
341 near sunrise in a way similar to the PRE near sunset. Fejer et al. (2008) found that the  
342 nighttime disturbance dynamo drifts are upward, and have the largest values near  
343 ~~rise~~sunrise. In our case, the model simulations and observations both show an  
344 increasing of the height of the ionosphere around sunrise. The enhancement of low-  
345 latitude ionospheric vertical plasma drift caused by DDEF and PPEF associated with  
346 the geomagnetic storm should play a vital role in triggering those EPBs. Our results

---

347 also provide evidence of the enhancement of low-latitude ionospheric vertical plasma  
348 drift around sunrise, which should be the main reason of the EPBs generation near dawn.  
349 In addition, some interesting features of EPBs are also shown in Figure 3 in that the  
350 EPBs showed also [bifurcation and merging processes](#). [Merging phenomenon of EPBs](#)  
351 [has been studied by some researchers \(Huang et al., 2012; Huba et al., 2015; Narayanan](#)  
352 [et al., 2016; Wu et al., 2017\)](#). ~~break and recombination processes. In Figure 6~~ [However,](#)  
353 [there is no study to report that bifurcation first and merging later occur in evolution of](#)  
354 [one EPBs. In Figure 7\(f\)](#), at latitude of 19°N, the zonal velocity of “b1” was about 60-  
355 70 m/s between 05:20 LT and 06:15 LT. However, at the latitude of 22°N (Figure ~~6~~7(d)),  
356 the zonal velocity of “b1” was decreased from about 70 m/s to about 50 m/s between  
357 05:20 LT and 05:45 LT. After 05:45 LT, its velocity began to increase from ~50 m/s to  
358 ~70 m/s from 05:45 LT to 06:00 LT. Then, it kept a velocity of ~70 m/s. Owing to the  
359 fact that the zonal velocity at higher latitudes was smaller than that at low latitudes  
360 before 05:45 LT, “b1” had a ~~break~~[bifurcation](#) process of EPBs during this period. After  
361 05:45 LT, the zonal velocity at higher latitude was bigger than that at lower latitude,  
362 “b1” exhibited a ~~recombination~~[merging](#) process of EPBs after 06:03 LT. The above  
363 results indicate that the ~~break~~[bifurcation](#) and ~~recombination~~[merging](#) processes of EPBs  
364 should be caused by the different drift velocities of the background plasma at different  
365 latitudes.

366

## 367 5. Summary

368 In this paper, a special EPB event was observed by an all-sky imager and the GNSS  
369 network in the southern China. The evolution processes and characteristics of those  
370 EPBs were studied in detail. Our main findings are summarized as below:

371 (1) The observed EPBs on 08 November 2015 emerged before sunrise and kept  
372 developing. They dissipated at about one hour after sunrise (~ after 08:00 LT) and  
373 the development stage lasted for at least about 3 hours. The evolution of EPBs  
374 developing around sunrise was observed for the first time by an all-sky imager and  
375 the GNSS network.

376 (2) They occurred in the recovery phase of a geomagnetic storm. The enhancement of

---

377 background ionospheric vertical plasma drift was also observed near sunrise. The  
378 rapid uplift of the ionospheric caused by the geomagnetic storm should be the main  
379 reason for triggering the EPBs.

380 (3) During the development, the EPBs drifted westward rather than eastward, The TIE-  
381 GCM simulation suggested that the westward drift of EPB is related to the westward  
382 disturbance winds.

383 (4) The EPB exhibited also ~~break~~bifurcation and ~~recombination~~merging processes  
384 during its development.

---

385 **Acknowledgement**

386 This work was supported by the Open Research Project of Large Research  
387 Infrastructures of CAS – “Study on the interaction between low/mid-latitude  
388 atmosphere and ionosphere based on the Chinese Meridian Project” and the Chinese  
389 Meridian Project, and the National Natural Science Foundation of China (41674152  
390 and 41331069). The airglow and digisonde data were downloaded from  
391 <http://data.meridianproject.ac.cn/>. The airglow data used in this study can be obtained  
392 by contacting the corresponding author. We acknowledge the use of GNSS data from  
393 the Crustal Movement Observation Network of China (CMONOC, [http:// neiscn.org/](http://neiscn.org/))  
394 and the data could be obtained upon request. We thank H. Liu from Macao University  
395 of Science and Technology for processing the GNSS data. [The development of the TEC  
396 process program is supported by the Science and Technology Development Fund,  
397 Macau SAR \(File no. 001/2016/AFJ and 0001/2019/A1\)](#). The IMF, AE, AL, AU, KP,  
398 and SYM/H data are obtained from the CDAWeb (<https://cdaweb.sci.gsfc.nasa.gov/>)  
399 and the WDC for geomagnetism at Kyoto University (<https://wdc.kugi.kyoto-u.ac.jp/>).  
400 The National Center for Atmospheric Research is sponsored by the National Science  
401 Foundation.

402

## References

- 403 Aa, E., Huang, W., Yu, S., Liu, S., Shi, L., & Gong, J., et al. (2015). [Chen,](#)  
404 [Y and Shen, H.:](#) A regional ionospheric tec mapping technique over china and  
405 adjacent areas on the basis of data assimilation. ~~*Journal of Geophysical Research:*~~  
406 ~~*Space Physics,*~~ [J. Geophys. Res.,](#) 120(6), 5049-5061,  
407 <https://doi.org/10.1002/2015JA021140>, 2015.
- 408 Aa, E., Huang, W., Liu, S., Ridley, A., Zou, S., Shi, L., et al. (2018). [Chen, Y., Shen, H.,](#)  
409 [Yuan, T., Li, J., and Wang, T.:](#) Midlatitude plasma bubbles over China and adjacent  
410 areas during a magnetic storm on 8 September 2017. *Space Weather,* 16, 321–  
411 331. <https://doi.org/10.1002/2017SW001776>, 2018.
- 412 Abdu, M. A. (2001). Outstanding problems in the equatorial ionosphere–  
413 thermosphere electrodynamics relevant to spread f. ~~*Journal of Atmospheric and*~~  
414 ~~*Solar Terrestrial Physics,*~~ [J. Atmos. Sol. Terr. Phys.,](#) 63(9), 869-884,  
415 [https://doi.org/10.1016/S1364-6826\(00\)00201-7](https://doi.org/10.1016/S1364-6826(00)00201-7), 2001.
- 416 Abdu, M. A. (2003). Magnetospheric disturbance induced equatorial plasma bubble  
417 development and dynamics: A case study in Brazilian sector. ~~*Journal of*~~  
418 ~~*Geophysical Research,*~~ [J. Geophys. Res.,](#) 108(A12),  
419 <https://doi.org/10.1029/2002ja009721>, 2003.
- 420 Basu, S., Basu, S., MacKenzie, E., Bridgwood, C., Valladares, C. E., Groves, K. M.,  
421 & Carrano, C. (2010). Specification of the occurrence of equatorial  
422 ionospheric scintillations during the main phase of large magnetic storms within  
423 solar cycle. *Radio Science,* 45, RS5009. <https://doi.org/10.1029/2009RS004343>,  
424 2010.
- 425 Blanc, M. & Richmond, A. D. (1980). The ionospheric disturbance  
426 dynamo. ~~*Journal of Geophysical Research: Space Physics,*~~ [J. Geophys. Res.,](#) 85(A4),  
427 <https://doi.org/10.1029/JA085iA04p01669>, 1980.
- 428 [Buhari, S. M. , Abdullah, M. , Hasbi, A. M. , Otsuka, Y. , Yokoyama, T. , & Nishioka,](#)  
429 [M.:](#) Continuous generation and two - dimensional structure of equatorial plasma  
430 bubbles observed by high - density gps receivers in southeast asia, [J. Geophys.](#)



---

431 [Res.,119, 12, https://doi.org/10.1002/2014JA020433, 2014.](https://doi.org/10.1002/2014JA020433)

432 Burke, W. J., Gentile, L. C., Huang, C. Y., Valladares, C. E., ~~&and~~ Su, S. Y. ~~.(2004).~~ [.:](https://doi.org/10.1029/2004JA010583)

433 Longitudinal variability of equatorial plasma bubbles observed by dmsp and

434 rocsat-1. ~~Journal of Geophysical Research,~~ [J. Geophys. Res.,](https://doi.org/10.1029/2004JA010583) 109(A12), 17-  
435 [https://doi.org/10.1029/2004JA010583, 2004.](https://doi.org/10.1029/2004JA010583)

436 Carter, B. A., Yizengaw, E., Pradipta, R., Retterer, J. M., Groves, K., ~~&~~ Valladares, C.,  
437 ~~et al.~~ ~~.(2016).~~ [Caton, R., Bridgwood, C., Norman, R., and Zhang, K.:](https://doi.org/10.1002/2015JA022194) Global  
438 equatorial plasma bubble occurrence during the 2015 St. Patrick's day  
439 storm. ~~Journal of Geophysical Research Space Physics,~~ [J. Geophys. Res.,](https://doi.org/10.1002/2015JA022194) 121(1),  
440 894-905. [https://doi.org/10.1002/2015JA022194, 2016.](https://doi.org/10.1002/2015JA022194)

441 Cherniak, I., ~~&and~~ Zakharenkova, I. ~~.(2016).~~ [.:](https://doi.org/10.1002/2016GL071421) First observations of super plasma  
442 bubbles in Europe. ~~Geophysical Research Letters,~~ [Geophys. Res. Lett.,](https://doi.org/10.1002/2016GL071421) 43,  
443 ~~11,~~137–11,145. [https://doi.org/10.1002/2016GL071421, 2016.](https://doi.org/10.1002/2016GL071421)

444 Dabas, R. S.,~~;~~ Singh, L.,~~;~~ Lakshmi, D. R.,~~;~~ Subramanyam, P. , Chopra, P. , ~~&and~~  
445 Garg, S. C. ~~.(2003).~~ [.:](https://doi.org/10.1029/2001RS002586) Evolution and dynamics of equatorial plasma bubbles:  
446 relationships to exb drift, postsunset total electron content enhancements, and  
447 equatorial electrojet strength. [Radio Science,](https://doi.org/10.1029/2001RS002586) 38(4), 1075-  
448 [https://doi.org/10.1029/2001RS002586, 2003.](https://doi.org/10.1029/2001RS002586)

449 Ding, F., Wan, W., Mao, T., Wang, M., Ning, B., Zhao, B., ~~&and~~ Xiong, B. ~~.(2014).~~ [.:](https://doi.org/10.1002/2014GL060107)

450 Ionospheric response to the shock and acoustic waves excited by the launch of the  
451 Shenzhou 10 spacecraft. ~~Geophysical Research Letters,~~ [Geophys. Res. Lett.,](https://doi.org/10.1002/2014GL060107) 41,  
452 3351–3358. [https://doi.org/10.1002/2014GL060107, 2004.](https://doi.org/10.1002/2014GL060107)

453 Eccles., ~~Vincent,~~ V. J. ~~.(1998).~~ [.:](https://doi.org/10.1029/98JA02657) A simple model of low-latitude electric fields. ~~Journal~~  
454 ~~of Geophysical Research,~~ [J. Geophys. Res.,](https://doi.org/10.1029/98JA02657) 103(A11), 26699-26708-  
455 [https://doi.org/10.1029/98JA02657, 1998.](https://doi.org/10.1029/98JA02657)

456 Fukao, S., Ozawa, Y., Yamamoto, M., and Tsunoda, R. T. ~~.(2003).~~ [.:](https://doi.org/10.1029/2003GL018383) Altitude extended  
457 equatorial spread F observed near sunrise terminator over Indonesia. [Geophys.](https://doi.org/10.1029/2003GL018383)  
458 [Res. Lett.,](https://doi.org/10.1029/2003GL018383) 30(22), 2137-[https://doi.org/10.1029/2003GL018383, 2003.](https://doi.org/10.1029/2003GL018383)

459 Fejer, B. G., ~~&and~~ Scherliess, L. ~~.(1998).~~ [.:](https://doi.org/10.1029/1998JA002657) Mid- and low-latitude prompt-penetration

460 ionospheric zonal plasma drifts. ~~*Geophysical Research Letters*~~, *Geophys. Res.*  
461 [Lett.](#), 25(16), 3071–3074. <https://doi.org/10.1029/98GL02325>, 1998.

462 Fejer, B. G., Scherliess, L., & Paula, E. R. D. (1999). Effects of the vertical plasma  
463 drift velocity on the generation and evolution of equatorial spread-f. ~~*Journal of*~~  
464 ~~*Geophysical Research Space Physics*~~, *J. Geophys. Res.*, 104, 19, 859–19, 869.  
465 <https://doi.org/10.1029/1999JA900271>, 1999.

466 Fejer, B. G., Souza, J. R., Santos, A. S., & Pereira, A. E. C. (2005). Climatology  
467 of F<sub>2</sub> region zonal plasma drifts over Jicamarca. ~~*Journal of Geophysical*~~  
468 ~~*Research*~~, *J. Geophys. Res.*, 110, A12310.  
469 <https://doi.org/10.1029/2005JA011324>, 2005.

470 Fejer, B. G., Jensen, J. W., & Su, S.-Y. (2008). Seasonal and longitudinal  
471 dependence of equatorial disturbance vertical plasma drifts. ~~*Geophysical Research*~~  
472 ~~*Letters*~~, *Geophys. Res. Lett.*, 35(20), <https://doi.org/10.1029/2008gl035584>,  
473 2008.

474 Garcia, F. J., Taylor, M. J., & Kelley, M. C. (1997). Two-dimensional spectral  
475 analysis of mesospheric airglow image data. *Applied Optics*, 36(29), 7374.  
476 <https://doi.org/10.1364/AO.36.007374>, 1997.

477 Haerendel, G., Eccles, J. V., & Çakir, S. (1992). Theory for modeling the equatorial  
478 evening ionosphere and the origin of the shear in the horizontal plasma flow.  
479 ~~*Journal of Geophysical Research*~~, *J. Geophys. Res.*, 97(A2), 1209–1223.  
480 <https://doi.org/10.1029/91JA02226>, 1992.

481 [Huang, C.-S., J. M. Retterer, O. de La Beaujardiere, P. A. Roddy, D. E. Hunton, J. O. Ballenthin,](#)  
482 [and R. F. Pfaff: Observations and simulations of formation of broad plasma depletions](#)  
483 [through merging process, \*J. Geophys. Res.\*, 117, A02314,](#)  
484 <https://doi.org/10.1029/2011JA017084>, 2012.

485 Huang, C. S., Beaujardiere, O. D. L., Roddy, P. A., Hunton, D. E., Ballenthin, J. O.,  
486 & Hairston, M. R. (2013). Long-lasting daytime equatorial plasma bubbles  
487 observed by the c/nofs satellite. ~~*Journal of Geophysical Research Space*~~

488 *Physics, J. Geophys. Res.*, 118(5), 2398-2408,  
489 <https://doi.org/10.1002/jgra.50252>, 2013.

490 ~~Huang, C. S. (2018).~~ Huang, C. S., and Roddy, P. A.: Effects of solar and geomagnetic  
491 activities on the zonal drift of equatorial plasma bubbles, *J. Geophys. Res.*, 121,  
492 628-637, <https://doi.org/10.1002/2015JA021900>, 2016.

493 Huang, C. S.: Effects of the postsunset vertical plasma drift on the generation of  
494 equatorial spread F, *Progress in Earth & Planetary Science*, 5(4), 3,  
495 <https://doi.org/10.1186/s40645-017-0155-4>, 2018.

496 Huba, J. D., T.-W. Wu, and J. J. Makela.: Electrostatic reconnection in the ionosphere, *Geophys.*  
497 *Res. Lett.*, 42, 1626–1631, <https://doi.org/10.1002/2015GL063187>, 2015.

498 Katamzi-Joseph, Z. T., Habarulema, J. B., & Hernández-Pajares, M. ~~(2017).~~  
499 Midlatitude postsunset plasma bubbles observed over Europe during intense  
500 storms in April 2000 and 2001, *Space Weather*, 15, 1177–1190,  
501 <https://doi.org/10.1002/2017SW001674>, 2017.

502 Kelley, M. C., Fejer, B. G., & Gonzales, C. A. ~~(1979).~~: An explanation for  
503 anomalous equatorial ionospheric electric fields associated with a northward  
504 turning of the interplanetary magnetic field. ~~*Geophysical Research*~~  
505 ~~*Letters*~~, *Geophys. Res. Lett.*, 6, 301-304,  
506 <https://doi.org/10.1029/GL006i004p00301>, 1979.

507 Kelley, M. C., ~~et al. (1986).~~ Labelle, J., Kudeki, E., Fejer, B. G., Basu, S., Baker, K. D.,  
508 Hanuise, C., Argo, P., Woodman, R.F., Swartz, W. E., Farley, D., and Meriwether,  
509 J.: The Condor Equatorial Spread F Campaign: Overview and results of the large-  
510 scale measurements. ~~*Journal of Geophysical Research*~~, *J. Geophys. Res.*, 91(A5),  
511 5487–5503, <https://doi.org/10.1029/JA091iA05p05487>, 1986.

512 Kelley, M. C. ~~(2009).~~: The Earth's Ionosphere: Plasma Physics and Electrodynamics,  
513 San Diego, CA: Academic, 2009.

514 Kil, H., Kintner, P. M., De Paula, E. R., & Kantor, I. J. ~~(2000).~~: Global positioning  
515 system measurements of the ionospheric zonal apparent velocity at cachoeira  
516 paulista in brazil. ~~*Journal of Geophysical Research Space Physics*~~, *J. Geophys.*

---

517 [Res.](https://doi.org/10.1029/1999JA000244) 105(A3), 5317-5327, <https://doi.org/10.1029/1999JA000244>, 2000.

518 Lühr H., Xiong, C., Park, J., ~~and~~ Rauberg, J. (2014).: Systematic study of  
519 ~~intermediatescale~~[intermediate scale](#) structures of equatorial plasma irregularities  
520 in the ionosphere based on CHAMP observations, *Front Phys.*, 2, 15,  
521 <https://doi.org/10.3389/fphy.2014.00015>, 2014.

522 Makela, J. J., Kelley, M. C., ~~&~~ ~~and~~ Nicolls, M. J. (2006).: Optical observations of  
523 the development of secondary instabilities on the eastern wall of an equatorial  
524 plasma bubble. ~~*Journal of Geophysical Research Space Physics*~~, *J. Geophys.*  
525 [Res.](https://doi.org/10.1029/2006JA011646) 111(A9), <https://doi.org/10.1029/2006JA011646>, 2006.

526 Makela, J. J., ~~and~~ Otsuka, Y. (2012).: Overview of Nighttime Ionospheric Instabilities  
527 at Low-and Mid-Latitudes: Coupling Aspects Resulting in Structuring at the  
528 Mesoscale, *Space Science Reviews*, 168, 419, [https://doi.org/10.1007/s11214-](https://doi.org/10.1007/s11214-011-9816-6)  
529 [011-9816-6](https://doi.org/10.1007/s11214-011-9816-6), 2012.

530 Martinis, C., Eccles, J. V., Baumgardner, J., Manzano, J., ~~&~~ ~~and~~ Mendillo, M. (2003).:   
531 Latitude dependence of zonal plasma drifts obtained from dual - site airglow  
532 observations. ~~*Journal of Geophysical Research Space Physics*~~, *J. Geophys.*  
533 [Res.](https://doi.org/10.1029/2002JA009462) 108(A3), <https://doi.org/10.1029/2002JA009462>, 2003.

534 [Narayanan, V. L., S. Gurubaran, and K. Shiokawa.: Direct observational evidence for the](#)  
535 [merging of equatorial plasma bubbles, \*J. Geophys. Res. Space Physics\*,121, 7923–7931,](#)  
536 <https://doi:10.1002/2016JA022861>, 2016.

537 Ott, E. (1978).: Theory of Rayleigh-Taylor bubbles in the equatorial ionosphere-  
538 ~~*Journal of Geophysical Research*~~, *J. Geophys. Res.*, 83(A5), 2066,  
539 <https://doi.org/10.1029/JA083ia05p02066>, 1978.

540 [Otsuka, Y., T. Aramaki, T. Ogawa, and A. Saito.: A statistical study of ionospheric](#)  
541 [irregularities observed with a GPS network in Japan, in \*Recurrent Magnetic\*](#)  
542 [Storms: Corotating Solar Wind Streams, \*Geophys. Monogr. Ser.\*, vol. 167, edited](#)  
543 [by B. T. Tsurutani et al., AGU, Washington, D. C, 2006.](#)

544 Park, S. H., England, S. L., Immel, T. J., Frey, H. U., ~~&~~ ~~and~~ Mende, S. B. (2007).: A  
545 method for determining the drift velocity of plasma depletions in the equatorial

546 ionosphere using far - ultraviolet spacecraft observations. *Journal of Geophysical*  
547 *Research—Space Physics*, J. Geophys. Res., 112(A11),  
548 <https://doi.org/10.1029/2007/JA012327>, 2007.

549 Pi, X., A. J. Mannucci, U. J. Lindqwister, and C. M. Ho.: Monitoring of global  
550 ionospheric irregularities using the worldwide GPS network, *Geophys. Res. Lett.*,  
551 24,18, 2283–2286, <https://doi.org/10.1029/97GL02273>, 1997.

552 Pimenta, A. A., Fagundes, P. R., Bittencourt, J. A., Sahai, Y., Gobbi, D., & Medeiros,  
553 A. F., ~~et al. (2001)~~. Taylor, M. J., and Takahashi, H.: Ionospheric plasma bubble  
554 zonal drift: a methodology using oi 630 nm all-sky imaging systems. *Advances in*  
555 *Space Research*, 27(6), 1219-1224, [https://doi.org/10.1016/s0273-](https://doi.org/10.1016/s0273-1177(01)00201-0)  
556 1177(01)00201-0, 2001.

557 Patra, A. K., Chaitanya, P. P., Dashora, N., Sivakandan, M., & Taori, A. ~~(2016)~~.  
558 Highly localized unique electrodynamic and plasma irregularities linked with the  
559 17 march 2015 severe magnetic storm observed using multitechnique common -  
560 volume observations from gadanki, india. *Journal of Geophysical Research Space*  
561 *Physics*, J. Geophys. Res., 121, 11,518-11,527,  
562 <https://doi.org/10.1002/2016JA023384>, 2016.

563 Sahai, Y., Becker-Guedes, F., Fagundes, P. R., de Jesus, R., de Abreu, A. J., Otsuka, Y.,  
564 ~~et al. (2009)~~. Shiokawa, k., Igarashi, K., Yumoto, K., Huang, C. S., Lan, H. T., Saito,  
565 A., Guarnieri, F. L., Pillat, V. G., and Bittencourt, J. A.: Effects observed in the  
566 ionospheric F region in the east Asian sector during the intense geomagnetic  
567 disturbances in the early part of November 2004. *Journal of Geophysical*  
568 *Research*, J. Geophys. Res., 114, A00A18,  
569 <https://doi.org/10.1029/2008JA013053>, 2009.

570 Santos, A. M., Abdu, M. A., Souza, J. R., Sobral, J. H. A., Batista, I. S., & Denardini,  
571 C. M. ~~(2016)~~. Storm time equatorial plasma bubble zonal drift reversal due to  
572 disturbance Hall electric field over the Brazilian region. *Journal of Geophysical*  
573 *Research: Space Physics*, J. Geophys. Res., 121, 5594–5612,  
574 <https://doi.org/10.1002/2015JA022179>, 2016.

- 
- 575 Sheehan, R. E., & Valladares, C. E. (2004). Equatorial ionospheric zonal drift  
576 model and vertical drift statistics from UHF scintillation measurements in South  
577 America. *Annales Geophysicae, Ann. Geophys.*, 22(9), 3177–3193.  
578 <https://doi.org/10.5194/angeo-22-3177-2004>, 2004.
- 579 Scherliess, L., & Fejer, B. G. (1997). Storm time dependence of equatorial  
580 disturbance dynamo zonal electric fields. *Journal of Geophysical Research: Space  
581 Physics, J. Geophys. Res.*, 102(A11), 24037–24046.  
582 <https://doi.org/10.1029/97ja02165>, 1997.
- 583 Taylor, M. J., Eccles, J. V., Labelle, J., & Sobral, J. H. A. (2013). High resolution  
584 oi (630 nm) image measurements of f - region depletion drifts during the guará  
585 campaign. *Geophysical Research Letters, Geophys. Res. Lett.*, 24(13), 1699-  
586 1702. <https://doi.org/10.1029/97g101207>, 2013.
- 587 Tulasi, R. S., Rama, R. P. V. S., Prasad, D. S. V. V. D., Niranjana, K., Gopi, K. S., &  
588 Sridharan, R., et al. (2008). Local time dependent response of postsunset esf  
589 during geomagnetic storms. *Journal of Geophysical Research Space Physics, J.  
590 Geophys. Res.*, 113, A07310. <https://doi.org/10.1029/2007/JA012922>, 2008.
- 591 Weber, E., Buchau, J., & Moore, J. (1980). Airborne studies of equatorial F layer  
592 ionospheric irregularities. *Journal of Geophysical Research, J. Geophys.  
593 Res.*, 85(A9), 4631–4641. <https://doi.org/10.1029/JA085iA09p04631>, 1980.
- 594 Xiong, C., Park, J., Lühr, H., Stolle, C., & Ma, S. Y. (2010). Comparing plasma  
595 bubble occurrence rates at CHAMP and GRACE altitudes during high and low  
596 solar activity. *Annales Geophysicae, Ann. Geophys.*, 28, 1647–1658.  
597 <https://doi.org/10.5194/angeo-28-1647-2010>, 2010.
- 598 Xiong, C., Lühr, H., & Fejer, B. G. (2015). Global features of the disturbance  
599 winds during storm time deduced from CHAMP observations. *Journal of  
600 Geophysical Research: Space Physics, J. Geophys. Res.*, 120, 5137–5150.  
601 <https://doi.org/10.1002/2015JA021302>, 2015.
- 602 Xiong, C., Stolle, C., Lühr, H., Park, J., Fejer, B. G., and Kervalishvili, G. N. (2016).  
603 Scale analysis of the equatorial plasma irregularities derived from Swarm

604 constellation, *Earth Planets Space*, 68, 121, [https://doi.org/10.1186/s40623-016-](https://doi.org/10.1186/s40623-016-0502-5)  
605 [0502-5](https://doi.org/10.1186/s40623-016-0502-5), [2016](#).

606 Xiong, C., Xu, J., Wu, K., & Yuan, W. (2018). Longitudinal thin structure  
607 of equatorial plasma depletions coincidentally observed by swarm constellation and  
608 all-sky imager. *Journal of Geophysical Research: Space Physics*, *J. Geophys.*  
609 *Res.*, 123(3), <https://doi.org/10.1002/2017JA025091>, [2018](#).

610 Wu, K., Xu, J., Wang, W., Sun, L., Liu, X., & Yuan, W. (2017). Interesting  
611 equatorial plasma bubbles observed by all-sky imagers in the equatorial region of  
612 China. *Journal of Geophysical Research*, *J. Geophys. Res.*, 122,  
613 <https://doi.org/10.1002/2017JA024561>, [2017](#).

614 Wu, K., Xu, J., Xiong, C., & Yuan, W. (2018). Edge plasma enhancements of  
615 equatorial plasma depletions observed by all-sky imager and the C/NOFS satellite.  
616 *Journal of Geophysical Research: Space Physics*, *J. Geophys. Res.*, 123, 8835-  
617 [8849](https://doi.org/10.1029/2018JA025809), <https://doi.org/10.1029/2018JA025809>, [2018](#).

618 Yang, Z., Song, S., Jiao, W., Chen, G., & Xue, J. (2016). Ionospheric  
619 tomography based on gnss observations of the cmonoc: performance in the topside  
620 ionosphere. *GPS Solutions*, 21(2), 363-375. [https://doi.org/10.1007/s10291-](https://doi.org/10.1007/s10291-016-0526-0)  
621 [016-0526-0](https://doi.org/10.1007/s10291-016-0526-0), [2016](#).

622 Zhang, R., Liu, L., Chen, Y., and Le, H. (2015). The dawn enhancement of the  
623 equatorial ionospheric vertical plasma drift. *Journal of Geophysical Research:*  
624 *Space Physics*, *J. Geophys. Res.*, 120, 688-697. [https://doi.org/10.1002/](https://doi.org/10.1002/2015JA021972)  
625 [2015JA021972](https://doi.org/10.1002/2015JA021972), [2015](#).

626 Zhang, R., Liu, L., Le, H., and Chen, Y. (2016). Evidence and effects of the sunrise  
627 enhancement of the equatorial vertical plasma drift in the F region ionosphere,  
628 *Journal of Geophysical Research: Space Physics*, *J. Geophys. Res.*, 121, 4826-  
629 [4834](https://doi.org/10.1002/2016JA022491), <https://doi.org/10.1002/2016JA022491>, [2016](#).

630 Zheng, J., Zhao, B., Xiong, B., & Wan, W. (2016). Spatial and temporal analysis  
631 of the total electron content over china during 2011-2014. *Advances in Space*  
632 *Research*, 57(12), <https://doi.org/10.1016/j.asr.2016.03.037>, [2016](#).

---

633 Zhou, Y. L., Lühr, Hermann, Xiong, C., & Pfaff, R. F. (2016). Ionospheric  
634 storm effects and equatorial plasma irregularities during the 17-18 march 2015  
635 event. *Journal of Geophysical Research: Space Physics*, *J. Geophys. Res.*, *121*,  
636 [9146-9163](https://doi.org/10.1002/2016JA023122), <https://doi.org/10.1002/2016JA023122>, 2016.



---

637 **Figure Captions**

638 **Figure 1.** The location of observation instruments. The red star denotes the geographic  
639 location of the all-sky imager at Qujing (25° N, 104° E). The blue circle denotes the  
640 field of view of the all-sky imager at an altitude of 250 km. The green dot denotes the  
641 geographic location of the digisonde at Fuke (19.5° N, 109.1° E). The red dotted line  
642 represents the magnetic equator.

643

644 **Figure 2.** (a)  $Kp$  indexes, (b) the interplanetary magnetic field (IMF)  $Bz$ , (c) SYM/H,  
645 and (d) AE, AU, AL during 06-08 November 2015. (e) The variations of h'F obtained  
646 from the digisonde at Fuke on 06-08 November 2015.

647

648 **Figure 3.** Images of equatorial plasma bubbles from the Qujing site between 05:15 LT  
649 and 06:21 LT on 08 November 2015. The observed images were mapped into  
650 geographical coordinates by assuming that the airglow emission layer was at an altitude  
651 of ~250 km. The white vertical line is a reference line of 106° E and horizontal line is  
652 a reference line of 25° N.

653

654 **Figure 4.** Total electron content residuals over China and adjacent areas with 10 minute  
655 interval during 04:30 – 08:20 LT on 08 November 2015. The black horizontal line is a  
656 reference line of 25° N.

657

658 **Figure 5.** ~~Total electron content residuals~~ [Two-dimensional map of absolute TEC during](#)  
659 [05:15 – 08:00 LT on 08 November 2015.](#)

660

661 [Figure 6.](#) [Two-dimensional map of rate of TEC index \(ROTI\)](#) correspond to each image  
662 of Figure 3. The black horizontal line is a reference line of 25° N. The black vertical  
663 line is a reference line of 106° E.

664

665 **Figure 6.** (a) N-S cross sections (between 104°E and 105°E) of the airglow images on

---

666 08 November 2015. (c) W-E cross sections (between 21.5°N and 22°N) of the airglow  
667 images. (e) W-E cross sections (between 18.5°N and 19°N) of the airglow images. (b)  
668 The variations of the meridian velocities of “b1” with local time. (d) and (f) The  
669 variations of the zonal velocities of “b1” at ~ 22°N and ~19°N geographical latitudes,  
670 respectively.

671

672 **Figure 78.** Contours of nighttime zonal winds at 250 km in a range from 0° to 40° N in  
673 latitude and from 90° to 120° E in longitude during 08 November 2015. The dashed  
674 rectangles represent the location of EPBs.

675

676 **Figure 89.** The ionograms observed by the digisonde at Fuke between 04:00 LT and  
677 07:30 LT on 08 November 2015.

678

679 **Figure 910.** The height of hmF2 in a range from 0° to 40° N in latitude and from 90°  
680 to 120° E in longitude during 08 November 2015. The red star represent the location of  
681 all-sky imager. The dashed rectangles represent the region of southeastern Qujing.

Figure 1

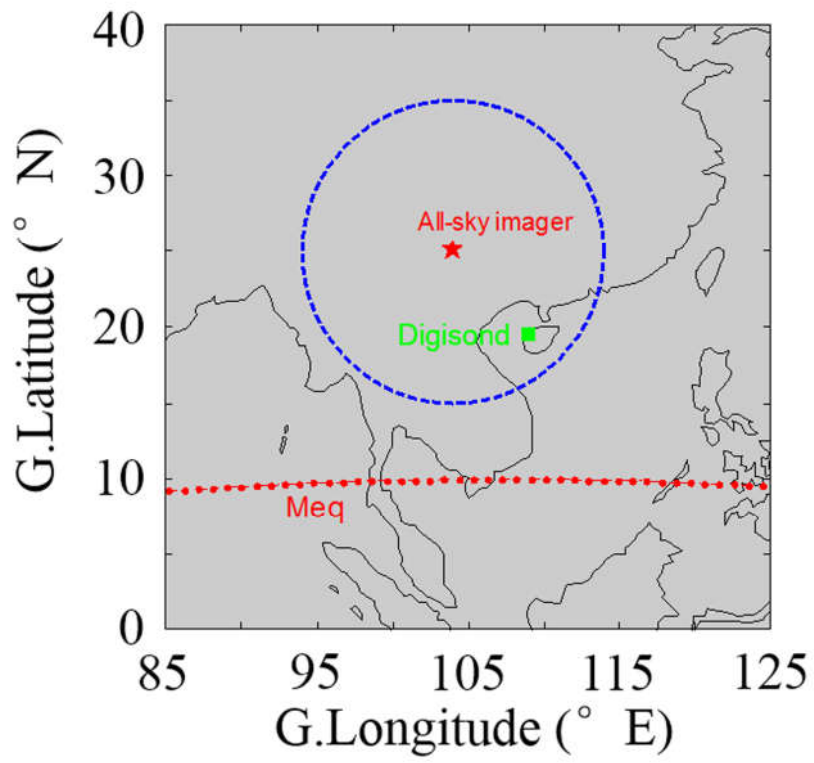


Figure 2

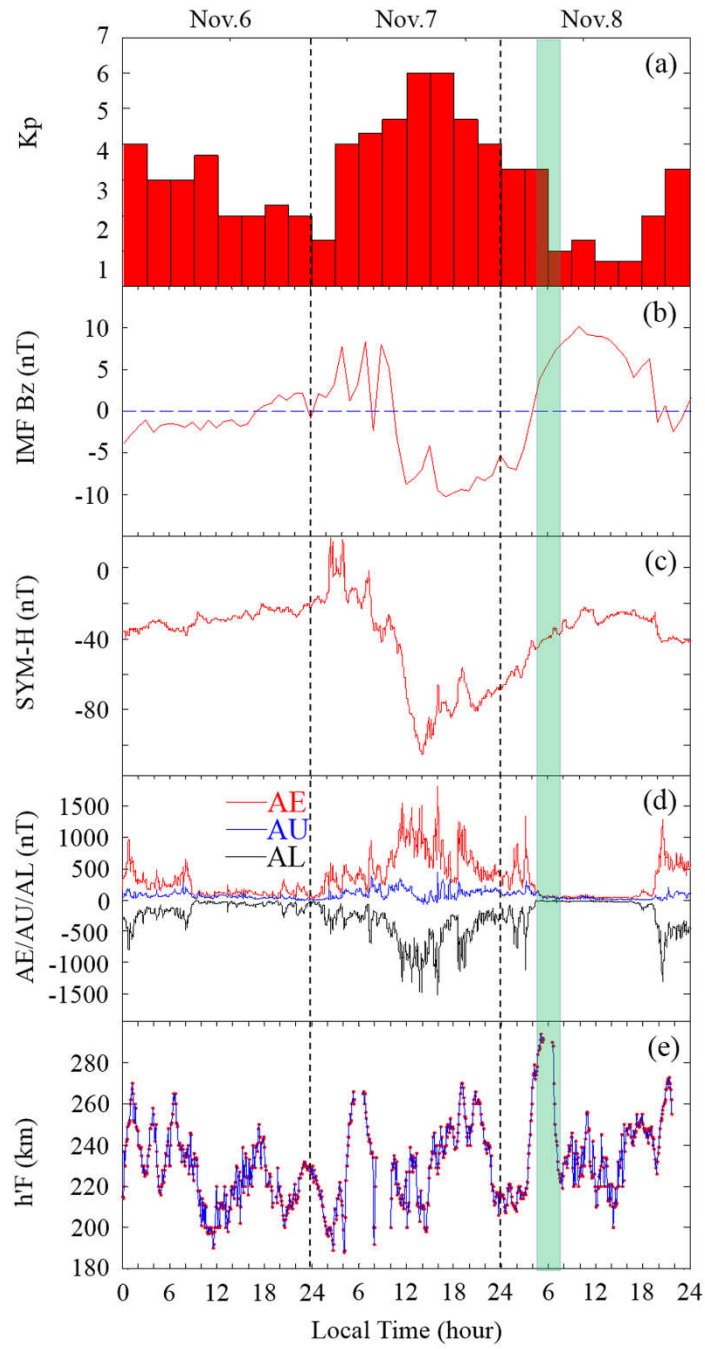


Figure 3

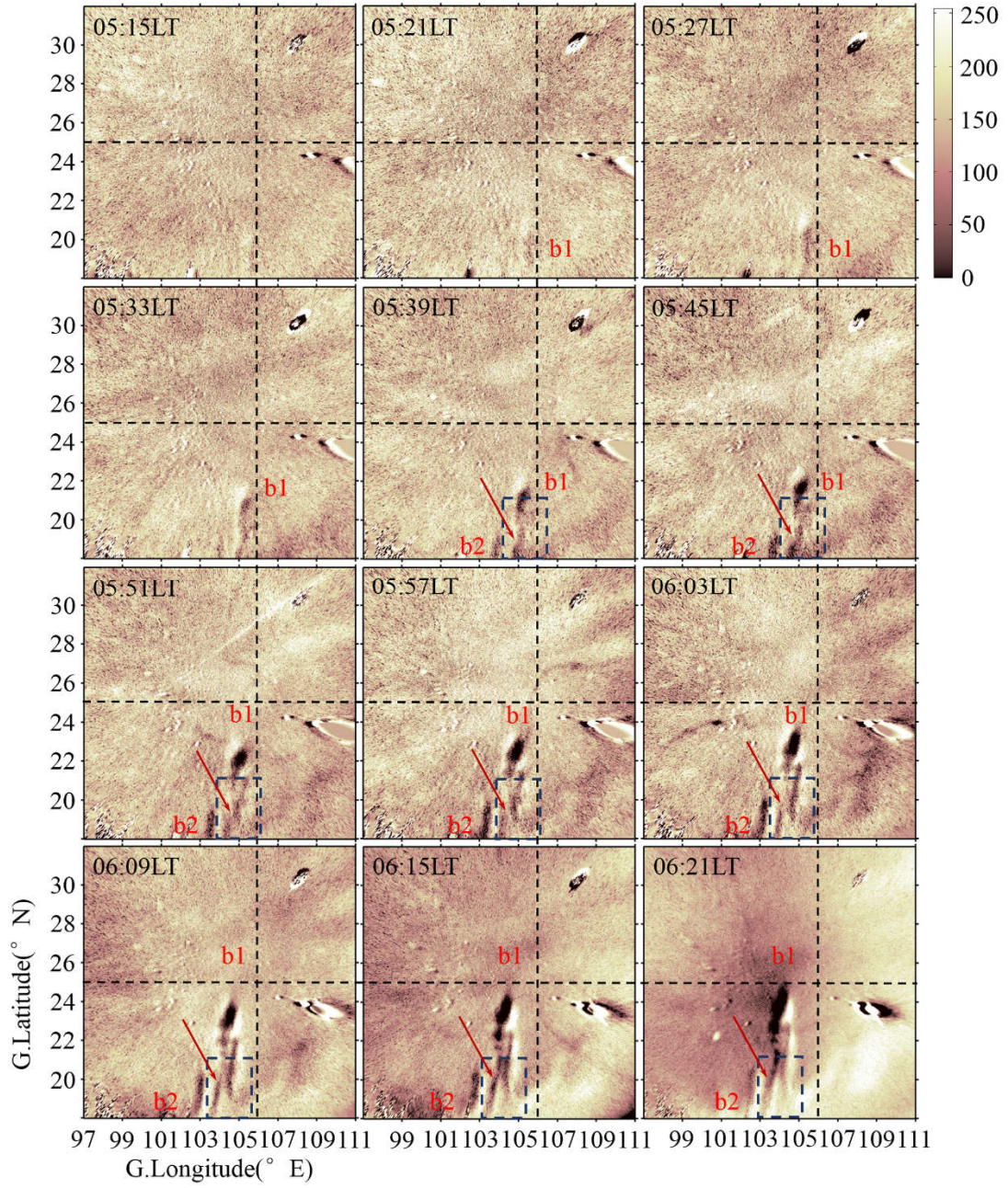




Figure 4

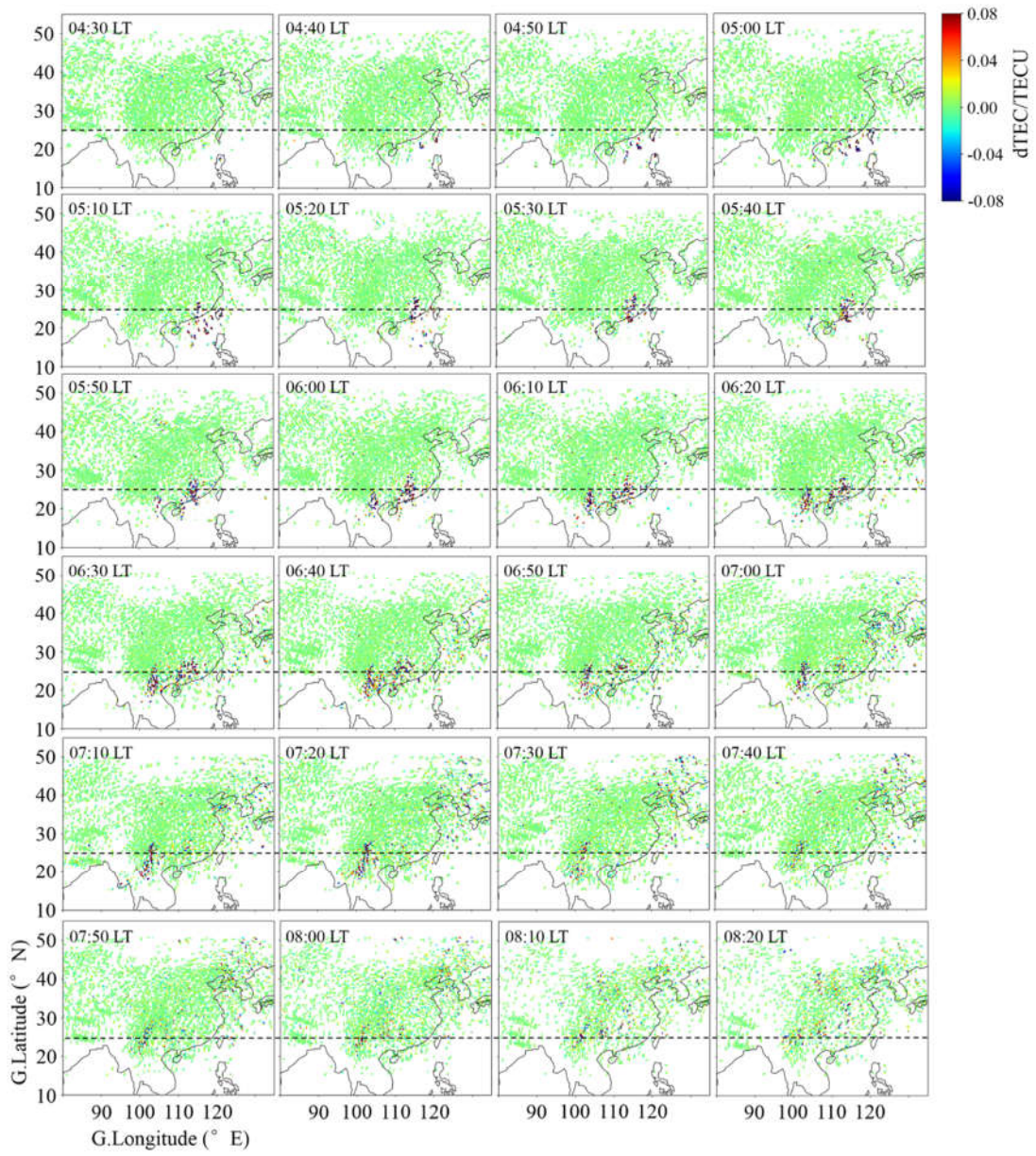
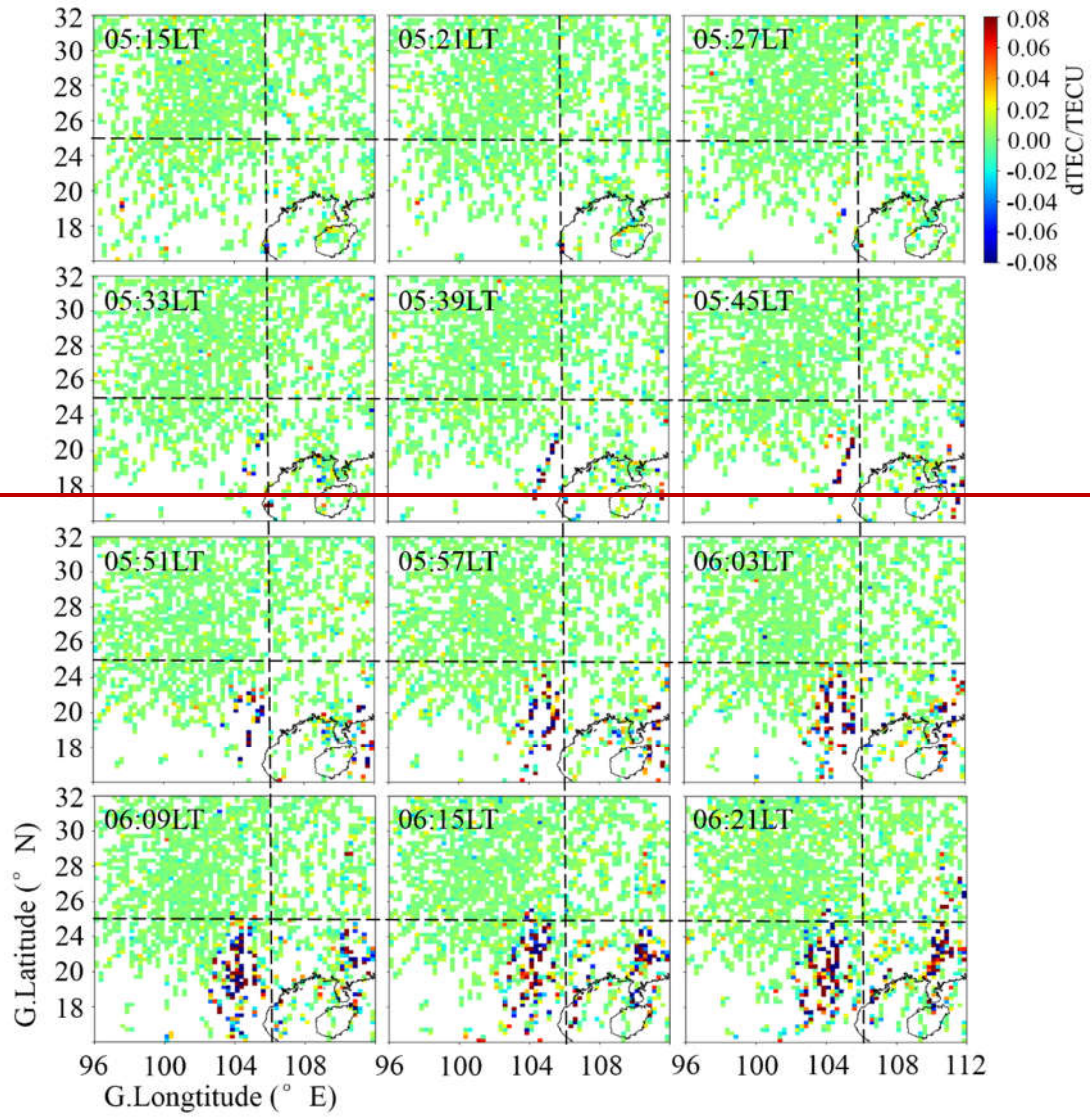


Figure 5





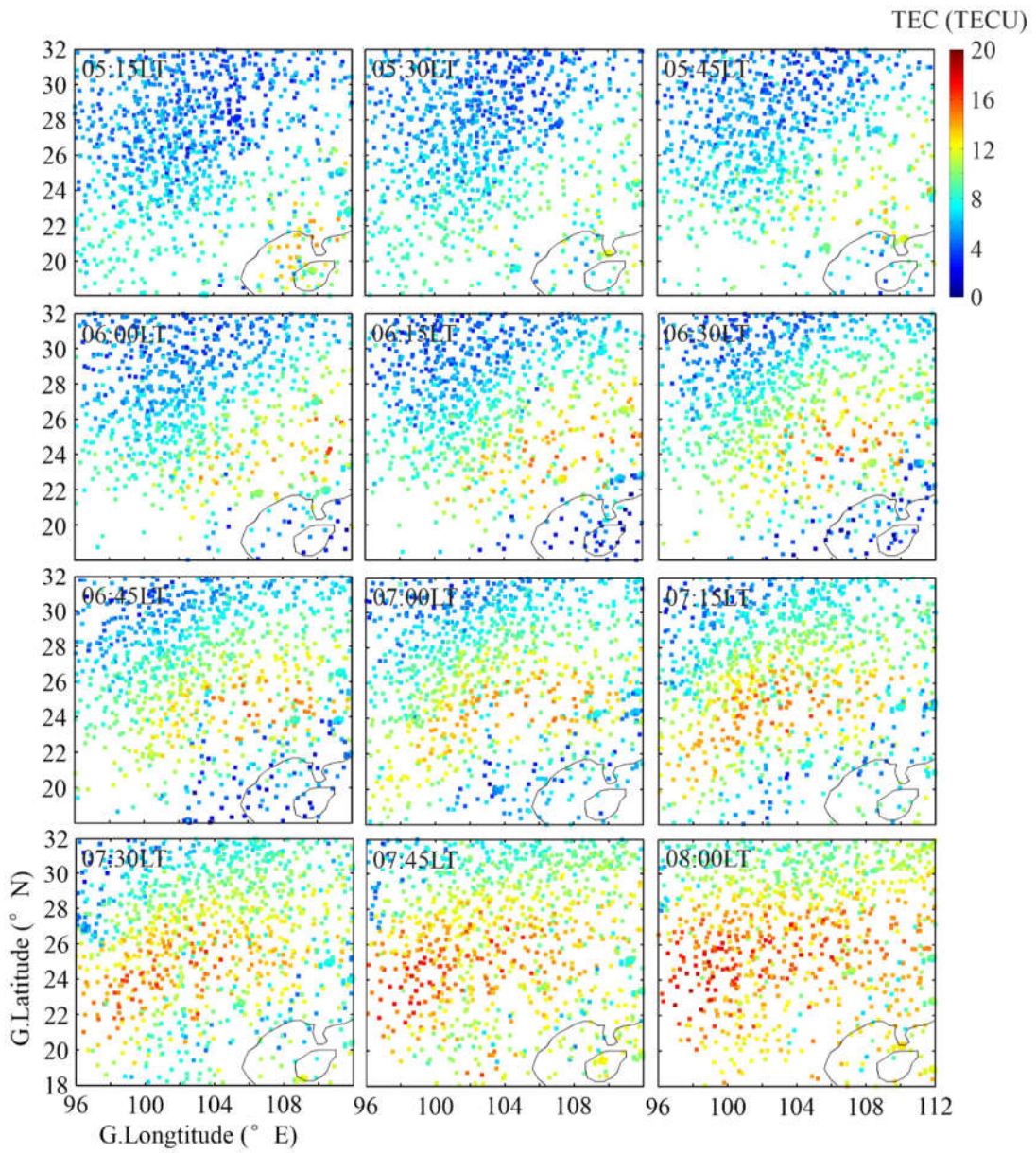
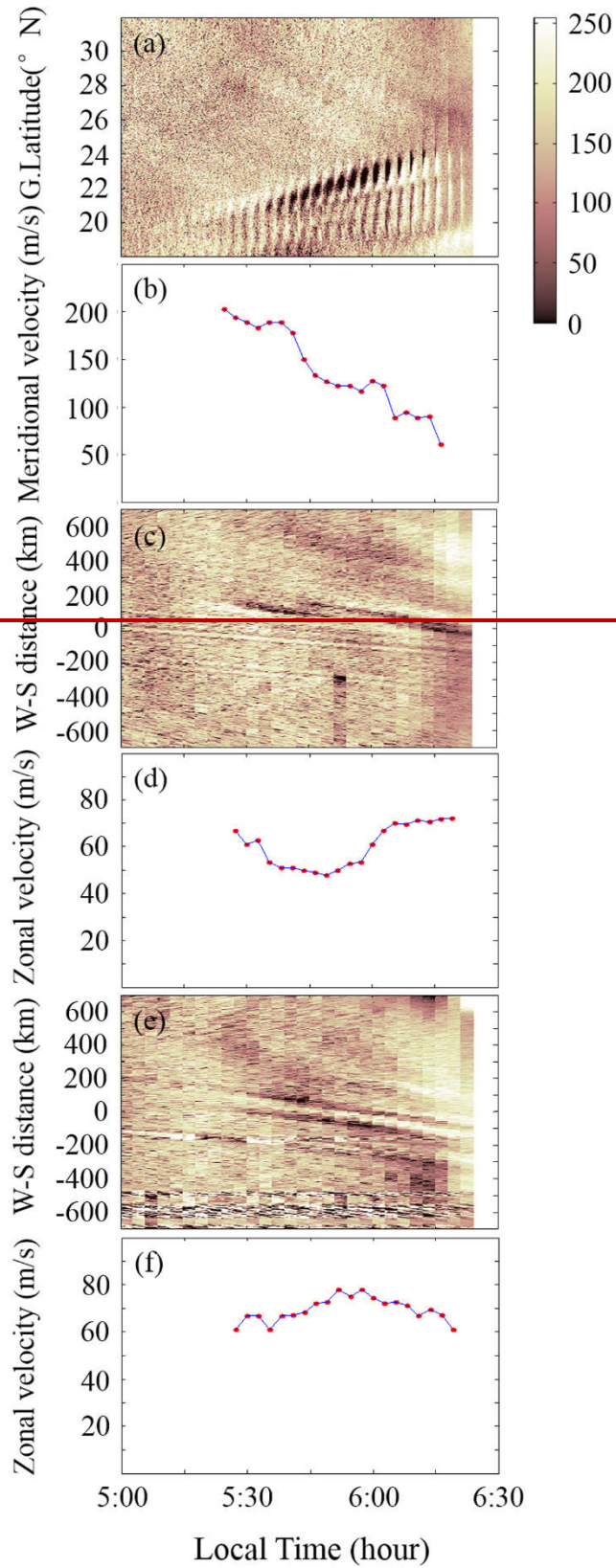




Figure 6



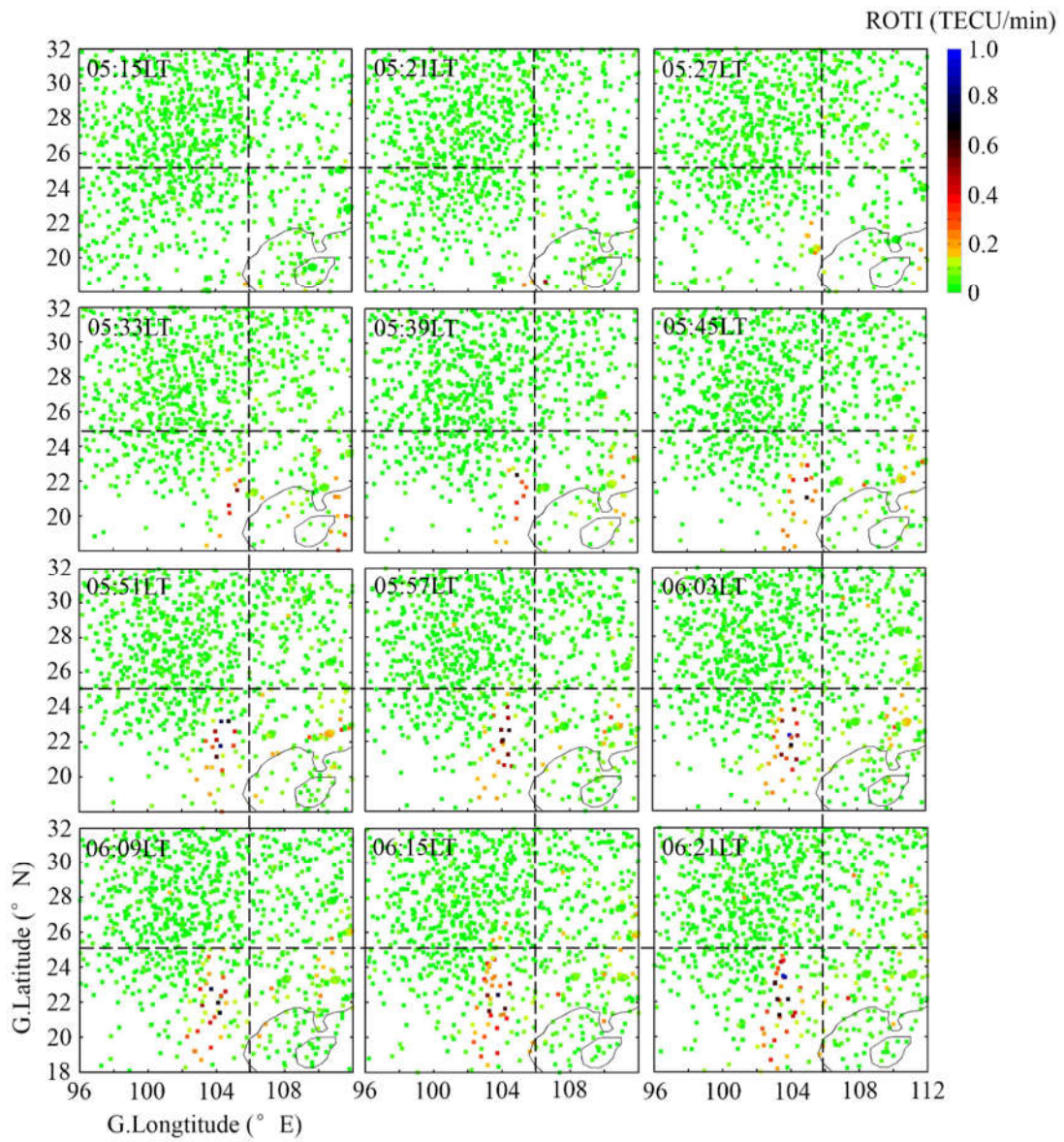
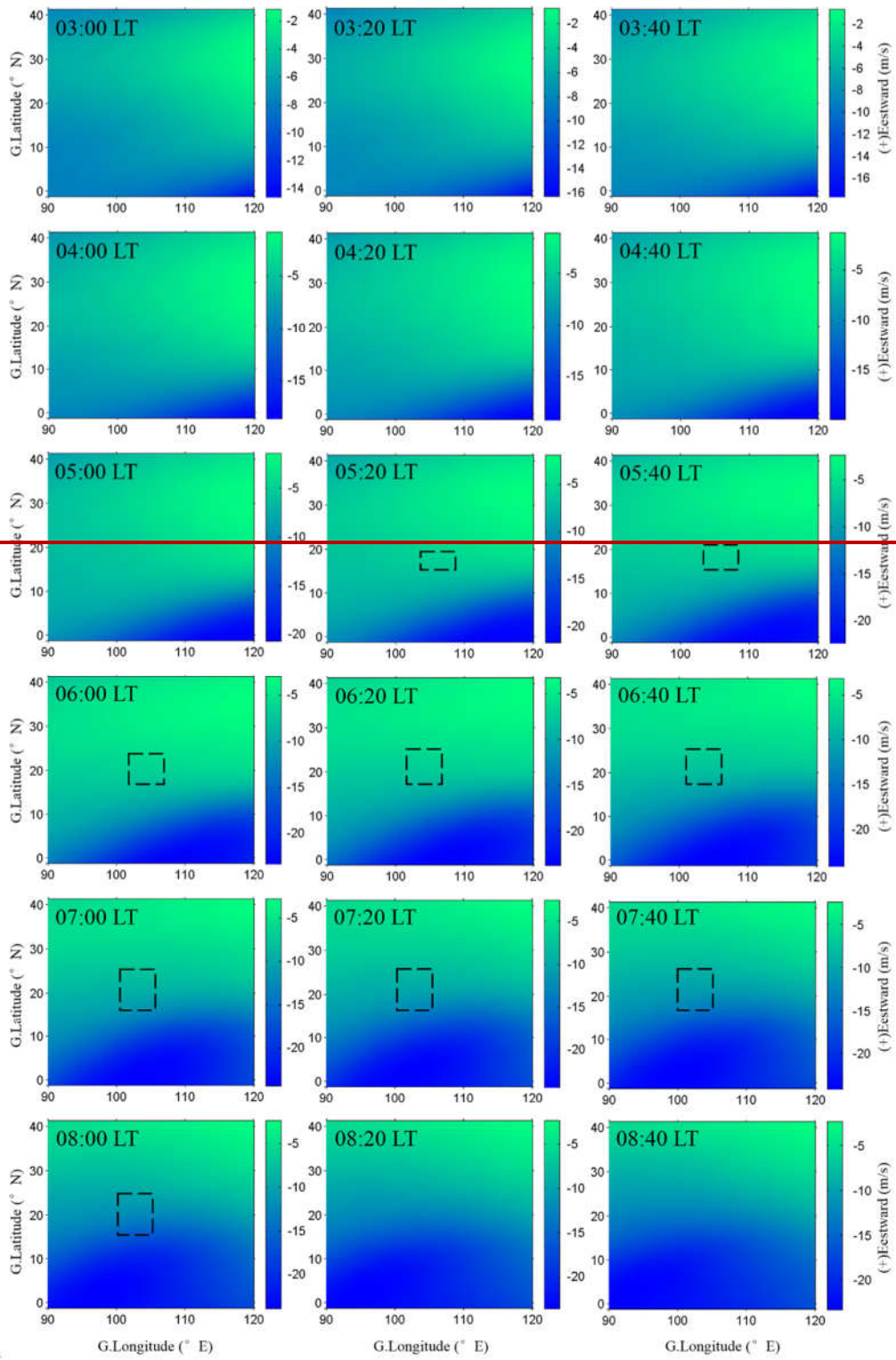


Figure 7





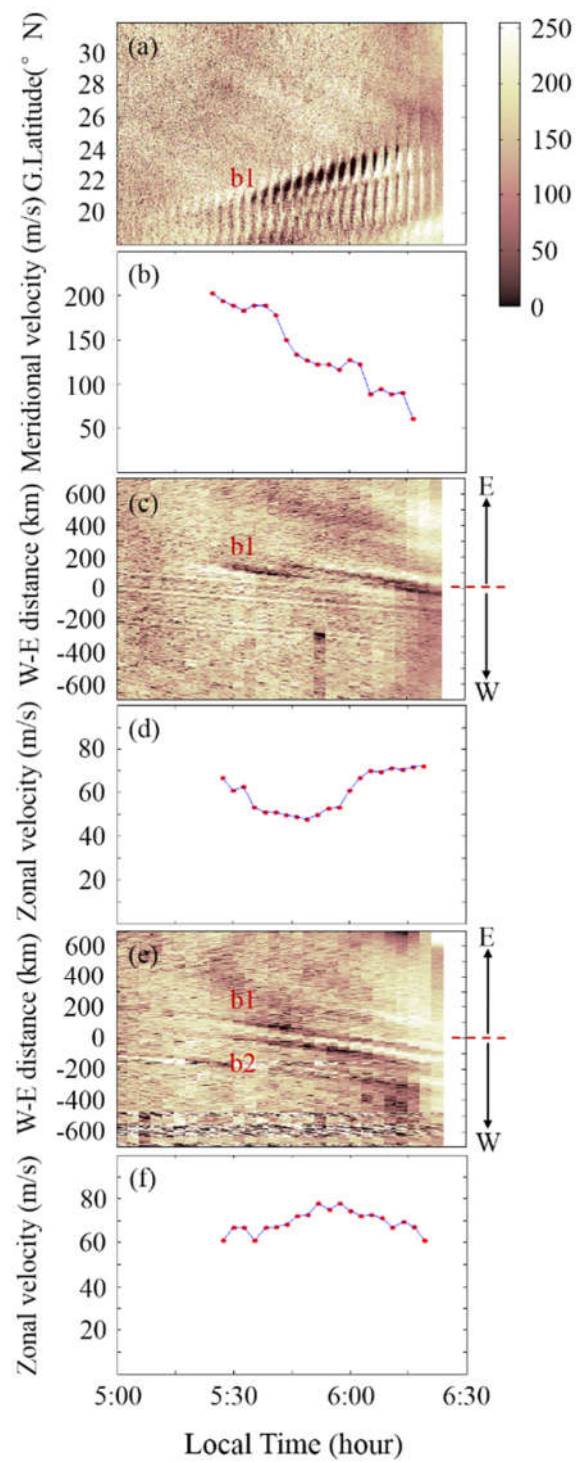


Figure 8

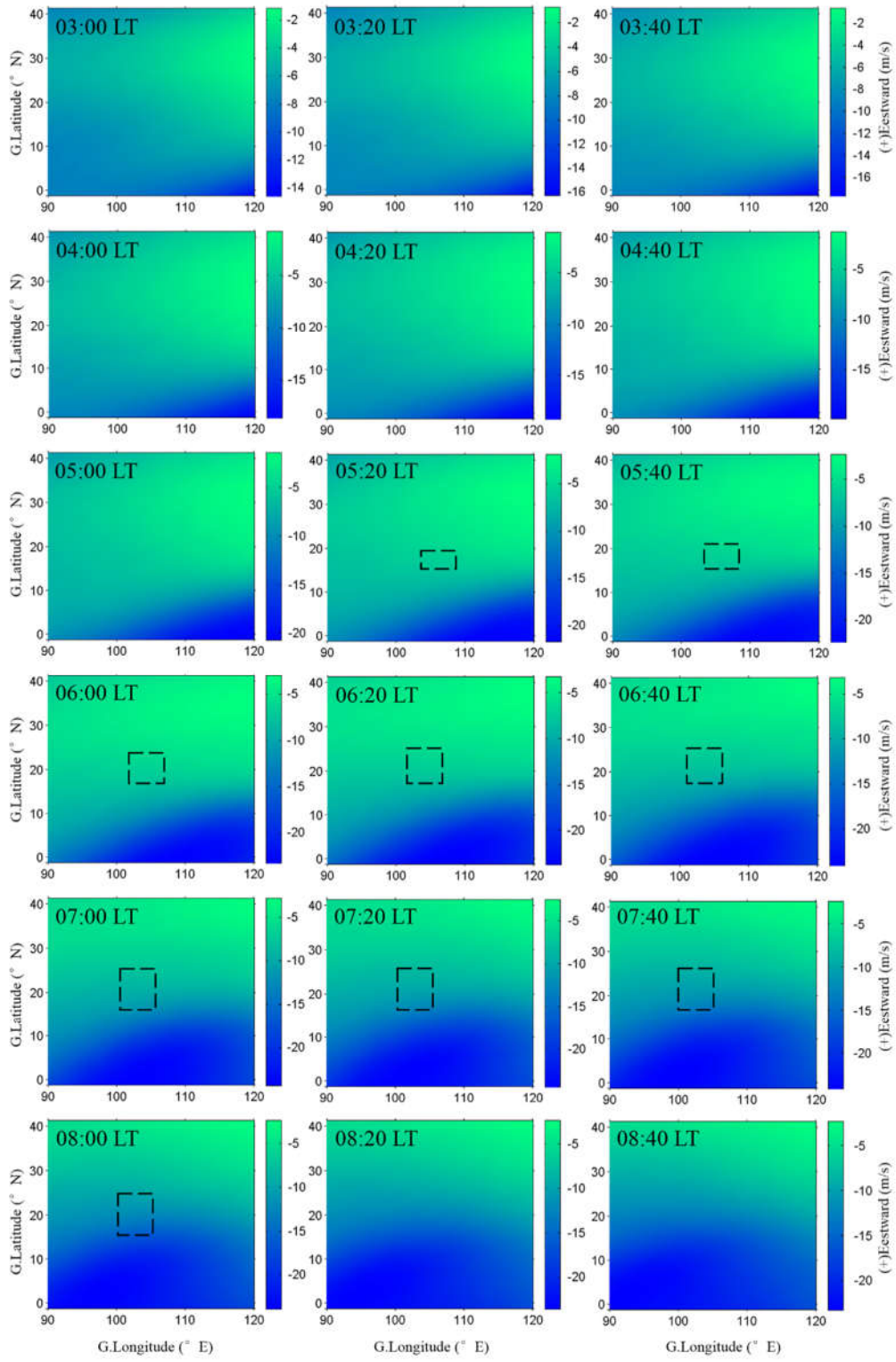


Figure 9

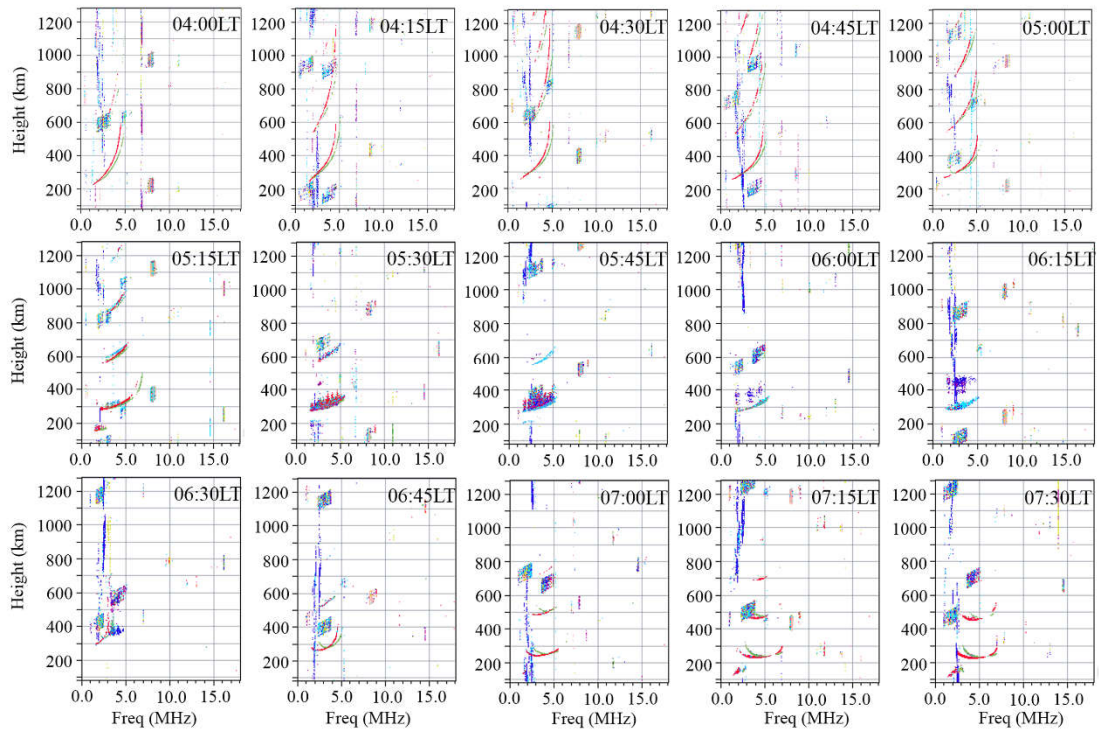


Figure 10

